Multi-instrument observation of nonlinear EMIC-driven electron precipitation at sub-MeV energies

A. T. Hendry[1], O. Santolik[1,2], C. A. Kletzing[3], C. J. Rodger[4], K. Shiokawa[5], D. Baishev[6]

[1]Department of Space Physics, Institute of Atmospheric Physics, Prague, Czechia
[2]Faculty of Mathematics and Physics, Charles University, Prague, Czechia
[3]Department of Physics and Astronomy, University of Iowa, Iowa City, Iowa, USA
[4]Department of Physics, University of Otago, Dunedin, New Zealand
[5]Institute for Space-Earth Environmental Research, Nagoya University, Nagoya, Japan
[6]Yu.G. Shafer Institute of Cosmophysical Research and Aeronomy of Siberian Branch of the Russian Academy of Sciences, Yakut Scientific Centre of Siberian Branch of the Russian Academy of Sciences, Yakutsk, Russia

Key Points:

- Closely correlated EMIC wave activity and sub-MeV electron precipitation is observed across multiple satellites.
- Both local and global dropouts in trapped electron flux are observed, down to hundreds of keV.
- Nonlinear test particle simulations show consistency between the observed electron precipitation and the observed wave.

Corresponding author: Aaron T. Hendry, `ath@ufa.cas.cz`

Abstract

In recent years, experimental results have consistently shown evidence of electromagnetic ion cyclotron (EMIC) wave-driven electron precipitation down to energies as low as hundreds of keV. However, this is at odds with the limits expected from quasi-linear theory. Recent analysis using nonlinear theory has suggested energy limits as low as hundreds of keV, consistent with the experimental results, although to date this has not been experimentally verified. In this study, we present concurrent observations from POES, RBSP, GPS, and ground-based instruments, showing concurrent EMIC waves and sub-MeV electron precipitation, and a global dropout in electron flux. We show through test particle simulation that the observed waves are capable of scattering electrons as low as hundreds of keV into the loss cone through nonlinear trapping, consistent with the experimentally observed electron precipitation.

1 Introduction

Electromagnetic Ion Cyclotron (EMIC) waves are Pc1-2 (0.1–5 Hz) pulsations that have long been known as a source of electron scattering loss from the radiation belts (e.g., Thorne & Kennel, 1971). Despite almost half a century of scientific inquiry, however, there are still basic characteristics of these interactions that we do not fully understand. In particular, the minimum electron energy at which these interactions are possible is still a matter of considerable debate. Determining this minimum interaction energy is crucial to better understanding the role that EMIC waves play in driving radiation belt dynamics and shaping the radiation belts as a whole.

Since the first direct experimental observations of EMIC-driven electron precipitation were made a decade ago (Miyoshi et al., 2008; Rodger et al., 2008), there has been a growing body of experimental observations of EMIC-driven electron precipitation. While some of these have been restricted to relativistic energies >2 MeV (e.g., Rodger et al., 2008; Usanova et al., 2014), a significant number of these observations have shown electron precipitation occurring at energies as low as a few hundred keV (e.g., Clilverd et al., 2015; Millan, Lin, Smith, & McCarthy, 2007; Rodger et al., 2015; Woodger et al., 2015). In particular, a recent study of hundreds of EMIC-driven electron precipitation events by Hendry, Rodger, and Clilverd (2017) showed the majority producing electron precipitation in the <1 MeV energy range.

These published experimental results are to a certain extent at odds with the dominant theory of EMIC-electron interactions. To date, the majority of theoretical investigations of EMIC-electron resonant scattering have used quasi-linear diffusion theory and typically estimate that, barring edge cases, EMIC-electron resonance is expected to be limited to energies >2 MeV (e.g., Meredith et al., 2003). However, recent studies using nonlinear theory have suggested that this energy could drop as low as ∼500 keV for waves very close to the ion cyclotron frequencies (e.g., Omura & Zhao, 2013), although to the authors' knowledge this has yet to be verified experimentally.

In this paper, we present a case study representing a remarkable simultaneous observation of EMIC waves and energetic electron precipitation by the Van Allen Probes (also known as the Radiation Belt Storm Probes – RBSP) and the Polar-orbiting Operational Environmental Satellite (POES) constellation, with supporting data from other spacecraft and ground-based instrumentation. These observations provide us with a unique opportunity to calculate the expected electron precipitation driven by the EMIC waves via test particle simulation, and directly compare these results to the precipitation observed by the POES spacecraft.

1.1 Instrumentation

We utilize magnetic field data from the RBSP Electric and Magnetic Field Instrument Suite and Integrated Science (EMFISIS), as well as pitch-angle resolved energy-dependent fluxes from the Energetic Particle, Composition, and Thermal Plasma (ECT) suite. The triaxial EMFISIS fluxgate magnetometer (MAG) samples the local magnetic field at 64 Hz, making it ideal for the study of EMIC waves. The ECT Magnetic Electron Ion Spectrometer (MagEIS) instrument measures pitch-angle resolved electron fluxes from 20–4800 keV, allowing a detailed look at the trapped electron flux near the satellite.

To complement the wave data from RBSP, we also investigate data from an Institute of Space-Earth Environmental Research (ISEE) 64 Hz ground-based induction coil magnetometer located in Zhigansk (ZGN), Russia(Shiokawa et al., 2017, 2010).

From POES, we investigate data from the MEPED instrument suite. We focus primarily on the 0°directional electron and proton telescopes, which ostensibly measures loss-cone particle fluxes. The electron telescope reports integral electron fluxes in three energy channels, > 30, > 100, and > 300 keV, named E1, E2, and E3 respectively. The proton telescope reports integral proton fluxes across 6 energy channels, from 30 to $>$ 6900 keV. A full description of the POES MEPED suite can be found in Evans and Greer (2000). We also make use of the ersatz E4 electron channel, an electron-contaminated proton channel which can be used to measure relativistic electron fluxes. A full description of the E4 channel can be found in Peck, Randall, Green, Rodriguez, and Rodger (2015).

We also use electron flux data from the Global Positioning System (GPS) Combined X-ray Dosimeter (CXD) instrument. The CXD instrument is carried by 21 GPS satellites, and reports electron flux over eleven energy channels from 140 keV to > 5.8 MeV (Cayton, 2004).

2 Case study

On 24 September 2016, at 19:51:22 UT, the POES NOAA-19 satellite observed a sudden burst of relativistic electron precipitation in each of the E1–E4 electron channel, shown in Figure 1(a), concurrently with a burst of energetic proton precipitation in the P1 proton channel. These bursts were flagged by the Carson, Rodger, and Clilverd (2013) EMIC detection algorithm as a potential EMIC-driven scattering event. At this time, the NOAA-19 satellite was located at $L = 5.0$ and 1.5 MLT, with a (IGRF+T89 (Tsyganenko, 1989)) footprint located at -50.8° N, 95.4° E. This precipitation burst was very short lived, lasting roughly 8 s and spanning $\Delta L = 0.15$. No energetic proton flux was observed in the P3–P5 channels, so contamination of the electron channels is assumed to be negligible.

Between 19:39–19:54 UT the RBSP-A EMFISIS instrument observed clear EMIC wave activity in the helium and hydrogen wave bands, between 0.25–0.55 Hz and 0.60–0.95 Hz respectively, either side of the hydrogen gyrofrequency; the y-component (field-aligned coordinates) of this wave is shown in Figure 1(c). At this time, the southern satellite footprint traced from -50.2° N, 93.0°E to -50.5°N, 92.5° E; in other words, at the time of the RBSP-A wave observations, the satellite was essentially collocated on the same field line as the NOAA-19 satellite. Examination of the EMFISIS Waves instrument places RBSP-A just inside the plasmapause at the event time. Rising-tone structures similar to those seen in Cluster data (e.g., Grison et al., 2013; Omura et al., 2010; Pickett et al., 2010) are clearly visible within the overall wave structure, primarily in the helium band.

From roughly 19:30–20:35 UT, concurrently with the RBSP observations, an IPDP-type EMIC wave was observed in the ZGN magnetometer (66.78N, 123.37E, $L = 4.4$), shown in Figure 1(d). As well as a gradual increase in overall wave frequency of ~ 0.4 Hz/hr, we see a number of fine-structure rising-tone elements within the wave, each lasting roughly 2 minutes.

Although the spatial separation of the ZGN magnetometer from the Northern footprint of the RBSP-A and POES satellites ($\sim \Delta 45°$ longitude) makes the causal relation between the two wave observations uncertain, EMIC waves are known to undergo significant ionospheric ducting (e.g., Manchester, 1966), allowing their detection far from the initial field-line footpoint. The similarities in the timing and frequency extent of the two wave observations suggest that these are indeed observations of the same wave. The EMFISIS-observed hydrogen-band wave is conspicuously absent from the ground-based observation, however we note that this is a known phenomenon (e.g., Usanova et al., 2008).

Coincident with this wave activity, the RBSP-A MagEIS instrument observed a sudden dropout in the trapped energetic electron flux. Although there is evidence of pitch-angle scattering at energies as low as ~ 150 keV, the dropout is clearest in the MagEIS energy channels from 346–1728 keV, with near simultaneous dropouts ranging from a factor of 2-9 observed across the channels. No dropout can be seen in the 2280 keV channel and above, although the fluxes are very low in these channels, which makes detecting a dropout difficult. The 597 keV channel is shown in Figure 1(e). We note a striking similarity between the MagEIS data seen in this event and that seen by Rodger et al. (2015), who observed five separate EMIC wave events in RBSP EMFISIS data, each resulting in a similar butterfly pitch-angle distribution as is seen in Figure 1(e).

Finally, we examined electron flux data from the GPS constellation CXD instruments to obtain a global picture of electron fluxes at the time of the EMIC event. The combined flux measurements of 21 GPS CXD instruments is plotted in Figure 1(f) for the E1–E4 (0.14–1.25 MeV) channels — in each channel we see clear dropouts in electron flux around $L = 5$ at the time of the EMIC wave event.

No chorus wave activity was observed by RBSP-A at the time of the EMIC wave event, ruling out chorus-driven scattering as the cause of the POES-observed precipitation. A small, weak burst of wave power in the chorus band was observed by RBSP-A shortly after 20 UT, however, as this wave activity occurred after the POES-observed precipitation and the RBSP- and GPS-observed flux dropouts, it cannot explain the observed electron precipitation.

At the time of the satellite observations none of the geomagnetic indices showed any sign of significant activity (Kp=2, Dst=3 nT, AE<200 nT). Activity appeared to increase in the hours following this event, however, with AE reaching 500 nT a few hours after the EMIC observations.

2.1 Event Analysis

To estimate the energy spectrum of the electron precipitation observed by POES, we use the method presented by Hendry et al. (2017) to fit a "peaked" spectral shape to the POES data. They found that this peaked spectrum was successful in reproducing EMIC-driven electron precipitation observed by the DEMETER and POES satellites, and so it is a good candidate for our current study. The result of this fitting process is shown in Figure 1(b). The peak electron flux appears to occur around 250 keV, with significant precipitation fluxes occurring between roughly 100–5000 keV, consistent with the results of Hendry et al. (2017). This is slightly lower than the expected minimum resonance energy of this wave – $\sim$400 keV (cf. Equation (12) of Omura and Zhao (2013)) – however this may be explained by the limitations of the POES fitting process.

This event does not lend itself to analysis using quasi-linear theory. The proximity of the wave-power to the helium gyrofrequency is not reconcilable with linear growth theory, which exhibits strong cyclotron damping near the ion gyrofrequencies (e.g., Chen, Thorne, & Horne, 2009). Nonlinear growth theory does not have such limitations, however, and has been shown to be capable of producing strong rising-tone emissions with wave-power very close to the ion gyrofrequencies (Shoji & Omura, 2013; Shoji et al., 2011). In addition to this, the scattering seen at high pitch-angles in the MagEIS data is not generally considered possible by EMIC waves (Usanova et al., 2014). However, the resulting butterfly pitch-angle distribution has been associated with nonlinear EMIC-driven scattering by Kubota and Omura (2017), who saw strong scattering of electrons near 90°

in their test-particle simulations due to nonlinear trapping, although primarily at relativistic energies. Butterfly distributions are also known to be produced by magnetopause shadowing and drift-shell splitting. However, as with the similar cases observed by Rodger et al. (2015), these are unlikely for this event due to the distance of the event from magnetic noon and due to negligible time-dispersion seen between the energies, respectively.

EMIC waves with rising-tone elements have been previously suggested as potential sources of significant rapid electron loss from the radiation belts due to nonlinear trapping (e.g. Omura & Zhao, 2013). Although it is difficult to determine the fine-structure of the wave, rising-tone elements can be seen. The wave data from the ZGN magnetometer, however, shows clear evidence of repeating rising-tone structure, suggesting that this wave may be a candidate for scattering due to nonlinear trapping.

Omura and Zhao (2012) show that nonlinear trapping by rising tone EMIC waves is possible for electrons that satisfy Equation (50) of Omura and Zhao (2012):

$$V_R - V_{tr} < v_{\parallel} < V_R + V_{tr} \tag{1}$$

where V_R is the cyclotron resonance velocity and V_{tr} is the trapping velocity, given by Equations (3) and (28) of Omura and Zhao (2013), respectively. Together, these define a range of velocities (and thus energies) for which nonlinear trapping is possible for a given EMIC wave. Figure 2(a) shows the range of electron energies and pitch-angles for which Equation (1) is true for any of the frequencies in the range 0.25–0.5 Hz, given a wave amplitude of 2.7 nT, calculated at the magnetic equator. Also shown in red is the minimum cyclotron resonant energy for each pitch-angle. It is clear from this figure that for this wave event nonlinear trapping is possible down to energies lower than the minimum cyclotron resonance energy, with a minimum nonlinear interaction energy of ~ 360 keV. At lower energies this interaction is restricted to smaller pitch-angles.

2.2 Test-particle simulation

To test the ability of the observed wave to scatter electrons into the loss-cone, we carry out a simple test-particle simulation. Following the example of Omura and Zhao (2013), we assume that the EMIC wave is generated at the equator and propagates parallel to the field line towards higher-latitudes in both directions according to:

$$\frac{\partial B_w}{\partial t} + V_g \frac{\partial B_w}{\partial z} = 0 \tag{2}$$

$$\frac{\partial \omega}{\partial t} + V_g \frac{\partial \omega}{\partial z} = 0 \tag{3}$$

$$\tag{4}$$

where B_w is the wave amplitude, ω is the wave frequency, z is the distance along the field line, and V_g is the group velocity given by Equation (23) of Omura et al. (2010). We use a 70:25:5 (H:He:O) ion composition ratio, with $n_e = 117\text{cm}^{-3}$ — following the example of Omura and Zhao (2013) we assume that the ion densities vary proportionally with the background magnetic field.

For this model we consider a dipole field line, scaled such that the magnetic field strength B calculated at RBSP-A's magnetic latitude is equal to the (background) magnetic field strength, measured by EMFISIS to be 138 nT. This gives an equatorial helium gyrofrequency of 0.51 Hz. We model the interaction between electrons and the wave field using Omura and Zhao's (2012) formulation of the relativistic equation of motion:

$$\frac{d\left(\gamma v_{\parallel}\right)}{dt} = v_{\perp}\Omega_w \sin\zeta - \frac{\gamma v_{\perp}^2}{2\Omega_e}\frac{\partial \Omega_e}{\partial z} \tag{5}$$

$$\frac{d\left(\gamma v_{\perp}\right)}{dt} = \left(\frac{\omega}{k} - v_{\parallel}\right)\Omega_w \sin\zeta + \frac{\gamma v_{\perp} v_{\parallel}}{2\Omega_e}\frac{\partial \Omega_e}{\partial z} \tag{6}$$

$$\frac{d\phi}{dt} = \frac{1}{\gamma v_{\perp}}\left(\frac{\omega}{k} - v_{\parallel}\right)\Omega_w \cos\zeta + \frac{\Omega_e}{\gamma} \tag{7}$$

where $v_{\parallel}$ and $v_{\perp}$ are the parallel and perpendicular velocity components, γ is the relativistic Lorentz factor, $\Omega_w = eB_w/m$, ζ is the difference between the wave and electron phase angles, $\Omega_e = eB/m$, and ϕ is the electron phase angle (e and m are the electron charge and mass, respectively).

We generate a set of test electrons such that the energy, pitch-angle, and phase space are each well-represented. We select a range of energies between 20–5000 keV; for each energy, we generate electrons from 5°–90° in pitch-angle and 5°–360° in phase, at discrete 5° intervals for both. These electrons are then initialised at the magnetic equator. If at any stage during the simulation the altitude of an electron drops below 100 km, we consider it to have been precipitated, and it is removed from further consideration. In total, we simulate 97,200 electrons.

We base our test wave-field on the combined observations from RBSP-A EMFISIS and the ZGN ground-based magnetometer. Although the wave consists of a series of consecutive rising-tone elements, we consider only a single wave element. This element increases linearly in frequency from 0.25–0.5 Hz (0.48–0.95 Ω_{He^+}) over the course of 120 seconds. For simplicity we assume a constant wave amplitude of 2.7 nT, based on the EMFISIS wave observations. The propagation of the wave is latitudinally limited by the local crossover frequency, which for this wave means MLAT < 30.

We note that, due to the one-dimensional nature of this simulation, we have excluded the effect of drift. We will discuss the implications of this later.

2.3 Simulation results

We start our simulation at 0 s, and run until the full wave element has been generated (120 s). Despite being out of resonance with the wave, early on in the simulation we see perturbations in the pitch-angle of the electrons as they pass through the wave. We believe that this is a manifestation of the non-resonant scattering phenomenon identified by Chen, Thorne, Bortnik, and Zhang (2016) – close examination of individual particle traces shows that this scattering occurs when the electron passes through the wavefront, matching the scattering process described by Chen et al. for non-resonant scattering. For electrons already very close to the loss cone, this scattering can result in the precipitation of the electron even at very low energies. In a realistic equatorial electron population, however, the electron population at pitch-angles close to the loss cone is typically very low, and is thus unlikely to have a significant effect on observed electron precipitation.

Although the pitch-angle scattering due to each non-resonant interaction is small, over the course of the simulation this scattering appears to cause a gradual shift in the trapped electrons' pitch angles towards the range ∼40-60°. The side-effects of this are two-fold. Firstly, this drives the creation of a butterfly distribution, due to the scattering of electrons away from 90°. Secondly, this drives electrons that are unable to be trapped by the wave down to pitch angles where nonlinear trapping is possible, into the region highlighted in Figure 2(a). This results in a much greater loss of electrons at lower energies than we might expect from just nonlinear trapping alone.

For electrons in resonance with the wave, we see very strong pitch-angle scattering characteristic of nonlinear trapping. This scattering often results in the rapid loss of the electron to the atmosphere within a small number of bounce periods. Due to the rising-tone nature of the wave, the point in the simulation where the electrons can reach resonance is strongly energy dependent; lower energy electrons can only reach resonance for wave frequencies very close to the ion gyrofrequency, and thus are scattered much later in the wave generation period. This rapid scattering is demonstrated in Figure 2(c), which shows the equatorial pitch-angle evolution of a sample of the test electrons. The higher energy electrons are scattered early in the simulation, while the lower energy electrons, much closer to the minimum nonlinear interaction energy, are only able to be trapped near the end of the simulation. Also evident is the pitch-angle drift of the higher pitch-angle electrons to lower pitch angles due to non-resonant interactions, where they are able to be nonlinearly trapped. This is particularly evident for the yellow trace, which shows a slow drift in pitch-angle from 80° to $\sim$ 50° over the course of the simulation, after which rapid nonlinear scattering occurs.

Figure 2(b) shows the evolution in time of the precipitated proportion of our test population. The energy dependence of the scattering is clearly evident, with the higher energy electrons scattering early in the wave generation period and the lower energy electrons following later. At the end of the wave generation period, roughly 80–90% of the test electrons with energies $>$ 1.5 MeV have been lost. For electron energies just below 1.5 MeV, the proportion of lost electrons slowly decreases. Below roughly 1 MeV the proportion of lost electrons begins to drop more rapidly, down to a minimum of $\sim$6% at the lowest energies, indicated by the dashed red line. We note that this corresponds almost entirely to the electrons initiated at a pitch angle of 5°, right at the edge of the loss cone, which make up 5400/97200 ($\sim$ 5.6%) of the simulated electrons. The rapid loss of these electrons appears to be purely due to non-resonant scattering.

To test the validity of this simulation we compare the results to the flux measurements made by the POES MEPED detectors. We generate a set of test particles such that the pitch angle and energy distributions reported by RBSP ECT before the wave onset are replicated. To ensure a close match to the data, we interpolate the ECT data to generate a 2D surface in pitch angle and energy space, then use an acceptance-rejection method to randomly generate 1,000,000 electrons. The distribution of these electrons in energy and pitch-angle is shown in Figure 3(a), with the spectrum summed across all pitch-angles over-plotted in white. We also generate a random initial phase for each electron, assuming that the electrons are uniformly distributed in phase. Finally, we extrapolate the results of our simulation to this new set of electrons, using a nearest neighbor approach to determine how long after wave onset the electron is expected to precipitate.

To estimate an electron energy spectrum for our simulation, we bin one second of simulated precipitation — the accumulation time of the POES MEPED detectors. As can be seen in Figure 1(c), the POES observed precipitation spike coincides roughly with the highest wave frequency in the rising tone element, so we use 119–120 s as our integration period. Figure 3(b) shows the comparison of the simulated electron energy spectrum and the POES-estimated spectrum from Section 2.1 — as we arbitrarily chose 1,000,000 particles to simulate, we have scaled the spectra to ensure similar flux ranges.

Figure 3(b) shows very close agreement between the POES data and our simulation at energies below $\sim$ 1000 MeV, with peak flux occurring at 250 and 400 keV respectively. Above 1 MeV, we see significantly less flux in the simulation results than is seen in the POES data. This is in part due to a weakness in the peaked energy spectrum used in Section 2.1, which tends to overestimate fluxes at ultra-relativistic energies. A more accurate energy spectrum would likely see an exponential decay in the flux after a certain energy (e.g., van de Kamp et al., 2016), however due to the limited data points available from the POES MEPED instrument, this level of detail is simply not possible without over-fitting the data.

We must also consider our exclusion of drift — in a full 3D simulation, some of the electrons lost due to EMIC scattering would be replenished by electrons drifting in from outside the event region. As higher energy electrons are both scattered earlier by the EMIC wave and drift faster, the lack of drift affects higher energy flux more than lower energy, and thus in a more realistic simulation we would expect to see more precipitation at higher energies across the simulation period, and hence a better agreement with the experimental measurements.

3 Summary and Discussion

We have observed an IPDP-type EMIC wave both in-situ and on the ground, with repeated rising-tone wave elements understood to be capable of driving rapid electron precipitation. We identify electron precipitation and a global electron flux dropout associated with this wave. Analysis of the POES-observed electron precipitation flux suggests an energy spectrum with precipitation down to ~ 100 keV, peaking at around 250 keV.

We test the ability of the wave to produce the observed precipitation with a simple one-dimensional test-particle simulation. We see rapid pitch-angle scattering characteristic of nonlinear trapping down to hundreds of keV, with reduced efficacy at lower energies. We also see evidence of non-resonant scattering, resulting in a shift of the electrons in pitch-angle away from 90°. Comparison between the simulation results and the POES-derived electron energy spectra shows remarkable similarities, with clear correlation in the peak precipitation energy.

To simplify our simulation, we did not allow for electron drift. However we can posit the effects that including this drift would have. Due to finite width of the EMIC source region and the rapid nature of the electron scattering that occurs at resonance, often on the order of 1-2 bounce periods, it is unlikely that drift would have a significant impact on the scattering of high energy electrons, nor on the lower energy electrons that were within the trapping region shown in Figure 2(a). Indeed, we would likely see an increase in the precipitation of higher energy electrons, due to the replenishing of the populations due to drift. However for lower energy electrons at high pitch-angles, where a pitch-angle shift due to non-resonant scattering is required to bring the electrons into the trapping region, we may see lower levels of precipitation, with the electrons drifting out of the source region before they can be scattered into the trapping region.

The inclusion of drift also helps to explain the global nature of the flux dropout observed by the GPS satellites. From the ground-based data, we know that the EMIC wave event was long-lived, lasting at least an hour, with the rising-tone elements repeating throughout this period. Given the drift periods of energetic and relativistic electrons at $L = 5$, this is sufficient for the entire trapped population to make multiple passes through the EMIC source region, resulting in the global dropout in electron flux seen in the GPS data.

The butterfly pitch-angle distribution that we observed in the MagEIS data appears to be a result of non-resonant scattering causing a slow shift of electrons in pitch-angle away from 90°. Interaction with repeated wave elements, such as those seen in the ZGN data, would exacerbate this effect. The rate of this pitch-angle shift may be exaggerated in this simulation due to the constant-amplitude wave used, leading to much sharper wave-fronts than might otherwise be seen in a more realistic simulation. Further investigation is needed to determine how this pitch-angle shift would change with a more realistic wave-model.

The electron precipitation observed in this event was likely driven into the loss cone due to a combination of nonlinear and non-resonant scattering by strong EMIC wave with rising-tone sub-elements. This result provides important context for the study by Hendry et al. (2017) who observed a significant population of EMIC-driven electron precipitation events in the sub-MeV energy range, but were unable to provide a conclusive answer as to the mechanism driving the precipitation. In the light of our results, it seems likely that nonlinear and non-resonant EMIC wave interactions explain a significant proportion of the lower-energy precipitation observed by Hendry et al. (2017).

This conclusion raises an interesting issue. If it was a simple matter of stronger waves scattering lower energy electrons, through nonlinear processes, then we would expect a bias towards the afternoon sector, where the strongest waves occur (e.g., Saikin et al., 2015). Instead, most studies of EMIC-driven electron precipitation (e.g., Hendry et al., 2017; Yahnin, Yahnina, Raita, & Manninen, 2017) identify the post-midnight MLT sector as the primary event location, where little wave activity is seen at all. It may be that the midnight region is preferentially associated with the generation of rising-tone EMIC waves, however further research is needed to determine if this is true.

Acknowledgments

The authors would like to thank the personnel who developed, maintain, and operate each of the satellites and instruments used in this study. Processing and analysis of the MagEIS and ECT data was supported by Energetic Particle, Composition, and Thermal Plasma (RBSP-ECT) investigation funded under NASAs Prime contract no. NAS5-01072. All RBSP-ECT data are publicly available at the web site http://www.rbsp-ect.lanl.gov/. Processing and analysis of EMFISIS data was performed under the support of JHU/APL contract no. 921647 under NASA Prime contract No. NAS5-01072. EMFISIS data may be obtained from http://emsis.physics.uiowa.edu/data/index. The POES MEPED data used in this study are publicly available at NOAA's National Geophysical Data Center (NGDC). The authors thank the CXD team at Los Alamos National Laboratory for their work on the GPS CXD data; the LANL-GPS particle data are publicly available, hosted by NOAA NCEI, and can be found through the data.gov website, or directly at http://www.ngdc.noaa.gov/stp/space-weather/satellite-data/satellite-systems/gps/. The induction coil magnetometer data used in this study is available at https://ergsc.isee.nagoya-u.ac.jp/data/ergsc/ground/geomag/stel/induction/. This work has been supported by the postdoctoral program of the Czech Academy of Sciences and by its Praemium Academiae award, the Ministry of Science and Higher Education of the Russian Federation and the Siberian Branch of the Russian Academy of Sciences (Project II.16.2.1, registration number AAAA-A17-117021450059-3), and by JSPS KAKENHI grants (25247080, 16H06286). OS also acknowledges support from grant LTAUSA17070.

References

Carson, B. R., Rodger, C. J., & Clilverd, M. A. (2013). POES satellite observations of EMIC-wave driven relativistic electron precipitation during 1998-2010. *Journal of Geophysical Research: Space Physics*, *118*(1), 232–243. Retrieved from `http://dx.doi.org/10.1029/2012JA017998` doi: 10.1029/2012JA017998

Cayton, T. E. (2004). *Monte carlo simulation of the particle channels of the cmobined x-ray sensor and dosimeter (CXD) for GPS block IIR and block IIF* (Tech. Rep.). Technical Report LA-UR-04-7092, Los Alamos National Laboratory, Los Alamos, NM, 87545, USA.

Chen, L., Thorne, R. M., Bortnik, J., & Zhang, X.-J. (2016). Nonresonant interactions of electromagnetic ion cyclotron waves with relativistic electrons. *Journal of Geophysical Research: Space Physics*, *121*(10), 9913–9925. Retrieved from `http://dx.doi.org/10.1002/2016JA022813` doi: 10.1002/2016JA022813

Chen, L., Thorne, R. M., & Horne, R. B. (2009). Simulation of emic wave excitation in a model magnetosphere including structured high-density plumes. *Journal of Geophysical Research: Space Physics*, *114*(A7). Retrieved from `https://agupubs.onlinelibrary.wiley.com/doi/abs/10.1029/2009JA014204` doi: 10.1029/2009JA014204

Clilverd, M. A., Duthie, R., Hardman, R., Hendry, A. T., Rodger, C. J., Raita, T., … Milling, D. K. (2015). Electron precipitation from EMIC waves: A case study from 31 May 2013. *Journal of Geophysical Research: Space Physics*, *120*(5), 3618–3631. Retrieved from `http://dx.doi.org/10.1002/2015JA021090` doi: 10.1002/2015JA021090

Evans, D. S., & Greer, M. S. (2000). *Polar Orbiting Environmental Satellite Space*

Environment Monitor-2: Instrument description and archive data documentation. US Department of Commerce, National Oceanic and Atmospheric Administration, Oceanic and Atmospheric Research Laboratories, Space Environment Center.

Grison, B., Santolk, O., Cornilleau-Wehrlin, N., Masson, A., Engebretson, M. J., Pickett, J. S., … Nomura, R. (2013). Emic triggered chorus emissions in cluster data. *Journal of Geophysical Research: Space Physics*, *118*(3), 1159-1169. Retrieved from `https://agupubs.onlinelibrary.wiley.com/doi/abs/10.1002/jgra.50178` doi: 10.1002/jgra.50178

Hendry, A. T., Rodger, C. J., & Clilverd, M. A. (2017). Evidence of sub-MeV EMIC-driven electron precipitation. *Geophysical Research Letters*, *44*(3), 1210–1218. Retrieved from `http://dx.doi.org/10.1002/2016GL071807` doi: 10.1002/2016GL071807

Kubota, Y., & Omura, Y. (2017). Rapid precipitation of radiation belt electrons induced by emic rising tone emissions localized in longitude inside and outside the plasmapause. *Journal of Geophysical Research: Space Physics*, *122*(1), 293-309. Retrieved from `https://agupubs.onlinelibrary.wiley.com/doi/abs/10.1002/2016JA023267` doi: 10.1002/2016JA023267

Manchester, R. N. (1966). Propagation of Pc 1 micropulsations from high to low latitudes. *Journal of Geophysical Research*, *71*(15), 3749–3754. Retrieved from `http://dx.doi.org/10.1029/JZ071i015p03749` doi: 10.1029/JZ071i015p03749

Meredith, N. P., Thorne, R. M., Horne, R. B., Summers, D., Fraser, B. J., & Anderson, R. R. (2003). Statistical analysis of relativistic electron energies for cyclotron resonance with EMIC waves observed on CRRES. *Journal of Geophysical Research: Space Physics*, *108*(A6). Retrieved from `http://dx.doi.org/10.1029/2002JA009700` doi: 10.1029/2002JA009700

Millan, R. M., Lin, R. P., Smith, D. M., & McCarthy, M. P. (2007). Observation of relativistic electron precipitation during a rapid decrease of trapped relativistic electron flux. *Geophysical research letters*, *34*(10).

Miyoshi, Y., Sakaguchi, K., Shiokawa, K., Evans, D., Albert, J., Connors, M., & Jordanova, V. (2008). Precipitation of radiation belt electrons by EMIC waves, observed from ground and space. *Geophysical Research Letters*, *35*(23). Retrieved from http://dx.doi.org/10.1029/2008GL035727 doi: 10.1029/2008GL035727

Omura, Y., Pickett, J., Grison, B., Santolik, O., Dandouras, I., Engebretson, M., ... Masson, A. (2010). Theory and observation of electromagnetic ion cyclotron triggered emissions in the magnetosphere. *Journal of Geophysical Research: Space Physics*, *115*(A7).

Omura, Y., & Zhao, Q. (2012). Nonlinear pitch angle scattering of relativistic electrons by EMIC waves in the inner magnetosphere. *Journal of Geophysical Research: Space Physics (1978–2012)*, *117*(A8).

Omura, Y., & Zhao, Q. (2013). Relativistic electron microbursts due to nonlinear pitch angle scattering by EMIC triggered emissions. *Journal of Geophysical Research: Space Physics*, *118*(8), 5008–5020.

Peck, E. D., Randall, C. E., Green, J. C., Rodriguez, J. V., & Rodger, C. J. (2015). POES MEPED differential flux retrievals and electron channel contamination correction. *Journal of Geophysical Research: Space Physics*, *120*(6), 4596–4612. Retrieved from http://dx.doi.org/10.1002/2014JA020817 doi: 10.1002/2014JA020817

Pickett, J. S., Grison, B., Omura, Y., Engebretson, M. J., Dandouras, I., Masson, A., ... Constantinescu, D. (2010). Cluster observations of emic triggered emissions in association with pc1 waves near earth's plasmapause. *Geophysical Research Letters*, *37*(9). Retrieved from http://dx.doi.org/10.1029/2010GL042648 doi: 10.1029/2010GL042648

Rodger, C. J., Hendry, A. T., Clilverd, M. A., Kletzing, C. A., Brundell, J. B., & Reeves, G. D. (2015). High-resolution in-situ observations of electron precipitation-causing emic waves. *Geophysical Research Letters*. Retrieved from http://dx.doi.org/10.1002/2015GL066581 doi: 10.1002/2015GL066581

Rodger, C. J., Raita, T., Clilverd, M. A., Seppälä, A., Dietrich, S., Thomson, N. R., & Ulich, T. (2008). Observations of relativistic electron precipitation from the radiation belts driven by EMIC waves. *Geophysical Research Letters*, *35*(16). Retrieved from http://dx.doi.org/10.1029/2008GL034804 doi: 10.1029/2008GL034804

Saikin, A. A., Zhang, J.-C., Allen, R., Smith, C. W., Kistler, L. M., Spence, H. E., ... Jordanova, V. K. (2015). The occurrence and wave properties of H+-, He+-, and O+-band EMIC waves observed by the Van Allen Probes. *Journal of Geophysical Research: Space Physics*. Retrieved from http://dx.doi.org/10.1002/2015JA021358 doi: 10.1002/2015JA021358

Shiokawa, K., Katoh, Y., Hamaguchi, Y., Yamamoto, Y., Adachi, T., Ozaki, M., ... others (2017). Ground-based instruments of the pwing project to investigate dynamics of the inner magnetosphere at subauroral latitudes as a part of the erg-ground coordinated observation network. *Earth, Planets and Space*, *69*(1), 160.

Shiokawa, K., Nomura, R., Sakaguchi, K., Otsuka, Y., Hamaguchi, Y., Satoh, M., ... Connors, M. (2010, Jun 01). The STEL induction magnetometer network for observation of high-frequency geomagnetic pulsations. *Earth, Planets and Space*, *62*(6), 517–524. Retrieved from https://doi.org/10.5047/eps.2010.05.003 doi: 10.5047/eps.2010.05.003

Shoji, M., & Omura, Y. (2013). Triggering process of electromagnetic ion cyclotron rising tone emissions in the inner magnetosphere. *Journal of Geophysical Research: Space Physics*, *118*(9), 5553-5561. Retrieved from https://agupubs.onlinelibrary.wiley.com/doi/abs/10.1002/jgra.50523 doi: 10.1002/jgra.50523

Shoji, M., Omura, Y., Grison, B., Pickett, J., Dandouras, I., & Engebretson, M. (2011). Electromagnetic ion cyclotron waves in the helium branch induced by multiple electromagnetic ion cyclotron triggered emissions. *Geophysical Research Letters*, *38*(17). Retrieved from https://agupubs.onlinelibrary.wiley.com/doi/abs/10.1029/2011GL048427 doi: 10.1029/2011GL048427

Thorne, R. M., & Kennel, C. F. (1971). Relativistic electron precipitation during magnetic storm main phase. *Journal of Geophysical research*, *76*(19), 4446–4453.

Tsyganenko, N. A. (1989). A magnetospheric magnetic field model with a warped tail current sheet. *Planetary and Space Science*, *37*(1), 5–20.

Usanova, M. E., Drozdov, A., Orlova, K., Mann, I. R., Shprits, Y., Robertson, M. T., ... Wygant, J. (2014). Effect of emic waves on relativistic and ultrarelativistic electron populations: Ground-based and van allen probes observations. *Geophysical Research Letters*, *41*(5), 1375–1381. Retrieved from http://dx.doi.org/10.1002/2013GL059024 doi: 10.1002/2013GL059024

Usanova, M. E., Mann, I. R., Rae, I. J., Kale, Z. C., Angelopoulos, V., Bonnell, J. W., ... Singer, H. J. (2008). Multipoint observations of magnetospheric compression-related EMIC Pc1 waves by THEMIS and CARISMA. *Geophysical Research Letters*, *35*(17). Retrieved from http://dx.doi.org/10.1029/2008GL034458 doi: 10.1029/2008GL034458

van de Kamp, M., Seppl, A., Clilverd, M. A., Rodger, C. J., Verronen, P. T., & Whittaker, I. C. (2016). A model providing long-term data sets of energetic electron precipitation during geomagnetic storms. *Journal of Geophysical Research: Atmospheres*, *121*(20), 12,520–12,540. Retrieved from http://dx.doi.org/10.1002/2015JD024212 doi: 10.1002/2015JD024212

Woodger, L. A., Halford, A. J., Millan, R. M., McCarthy, M. P., Smith, D. M., Bowers, G. S., ... Liang, X. (2015). A summary of the BARREL campaigns: Technique for studying electron precipitation. *Journal of Geophysical Research: Space Physics*, *120*(6), 4922–4935. Retrieved from http://dx.doi.org/10.1002/2014JA020874 doi: 10.1002/2014JA020874

Yahnin, A. G., Yahnina, T. A., Raita, T., & Manninen, J. (2017). Ground pulsation magnetometer observations conjugated with relativistic electron precipitation. *Journal of Geophysical Research: Space Physics*, *122*(9), 9169-9182. Retrieved from https://agupubs.onlinelibrary.wiley.com/doi/abs/10.1002/2017JA024249 doi: 10.1002/2017JA024249

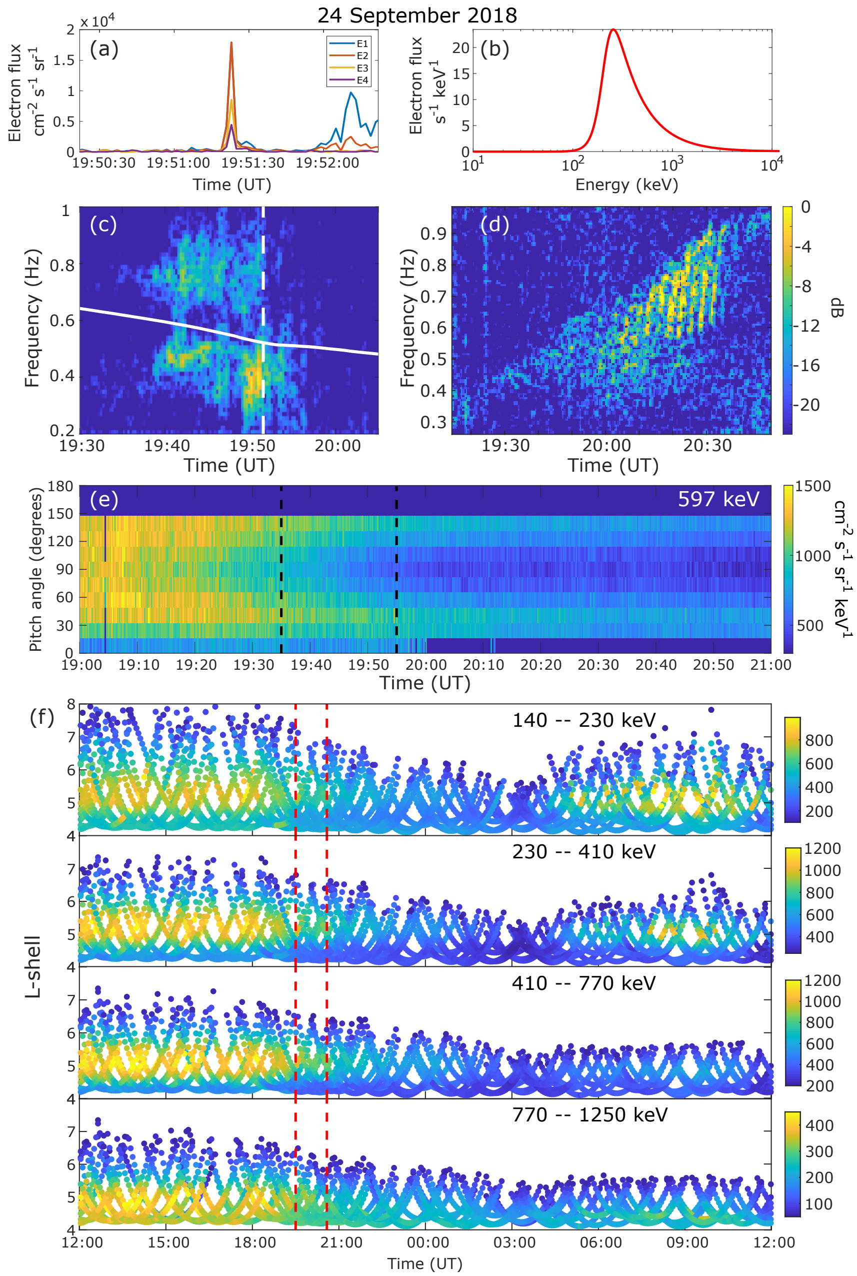

Figure 1. (a) POES MEPED 0° E1–E4 flux, showing clear electron precipitation spikes indicative of EMIC wave activity. Note that the E1 and E2 spikes are identical, and so the E1 spike is not visible in this plot. (b) Estimated POES MEPED electron precipitation flux spectrum, with peak flux occurring at roughly 250 keV. (c) Spectrogram of the y-component (field-aligned coordinates) of the RBSP EMFISIS magnetic field data at the time of the POES precipitation spike (white dashed line), with a solid white line indicating the He^+ gyrofrequency. (d) Spectrogram of the dD/dt component of the ZGN induction magnetometer, showing clear rising-tone elements. (e) RBSP ECT MagEIS pitch-angle resolved electron flux at the event time. The black dashed lines indicate the period of wave activity as seen in the EMFISIS instrument. (f) Combined electron flux observations from the 21 GPS CXD instruments, across the E1–E4 (140–1250 keV) channels. The red dashed lines indicate the extent of the EMIC wave activity as seen from the ZGN magnetometer.

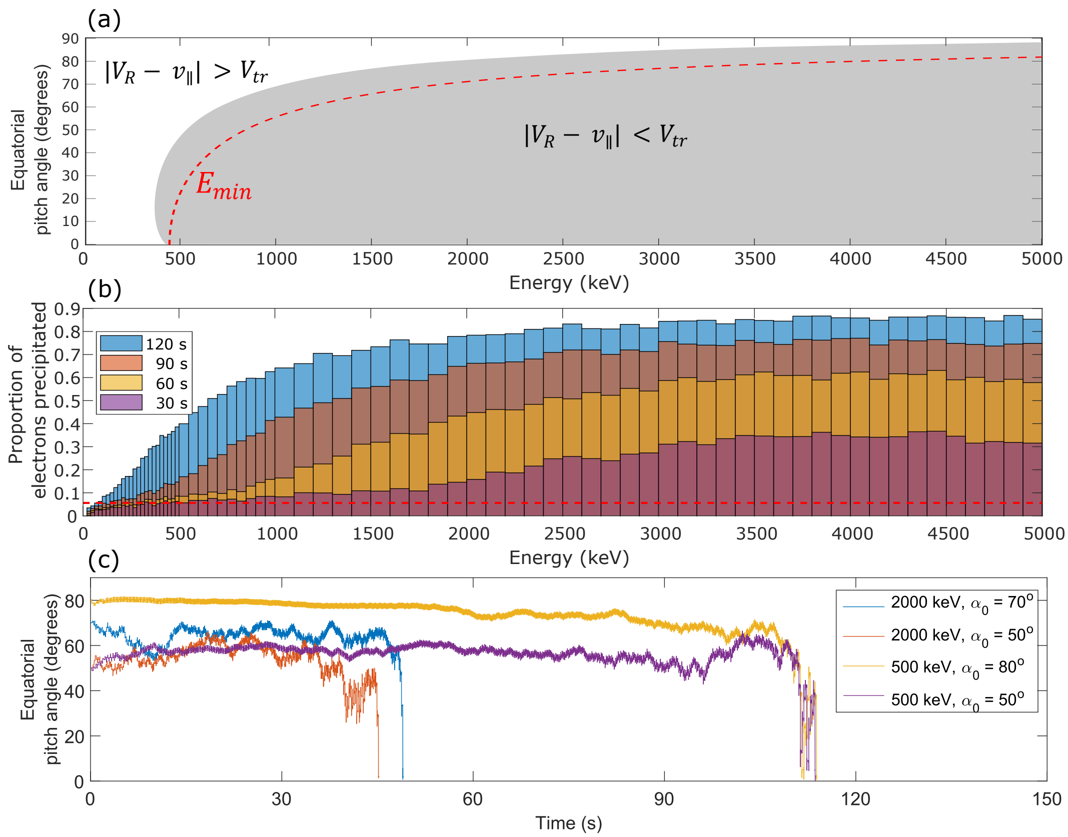

Figure 2. (a) Depiction of the region in pitch-angle and energy-space for which Equation (1) holds and thus nonlinear trapping is possible, calculated at the magnetic equator, with the minimum resonant energy shown in red. (b) Evolution of the equatorial pitch angles of a sample of the precipitated test electrons. (c) Evolution of the precipitated population of the test electrons, binned by energy, at 30, 60, 90, and 120 s. The red dashed line indicates the electron population initially located just outside the bounce loss cone, which are rapidly lost due to stochastic scattering.

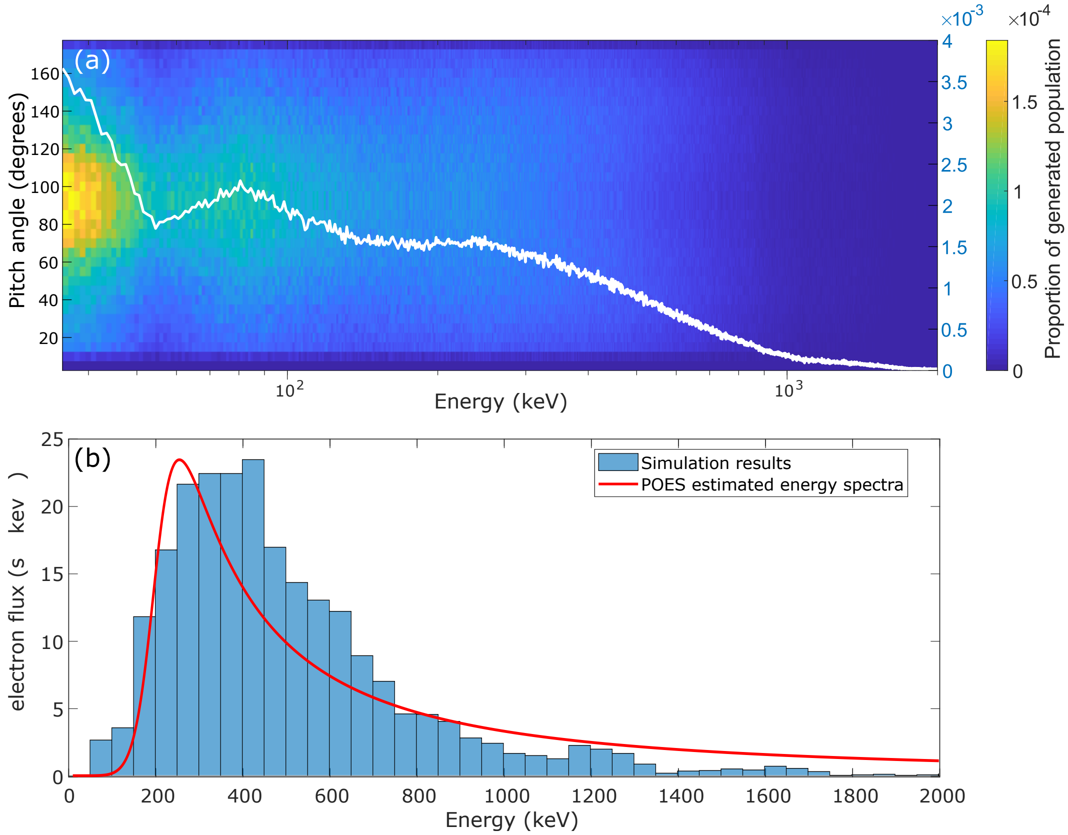

Figure 3. (a) Distribution of the generated electrons in energy and pitch-angle. The white line represents the energy spectrum of this distribution summed across all pitch-angles. The scales on the right represent the proportion of the total generated electron population. (b) Comparison of the POES-derived electron precipitation flux spectrum (red line) with the precipitation predicted by the test particle simulation between 119–120 s (cyan histogram).